

Numerical study of hybrid nanofluid flow and heat transfer on a stretching sheet with MHD and heat generation effects

Vemula Rajesh¹ | Mandava Srilatha¹ | Ali J. Chamkha²

¹Department of Mathematics, GITAM (Deemed to be University), Hyderabad Campus, Patancheru (M), Medak, Telangana, India

²Faculty of Engineering, Kuwait College of Science and Technology, Doha, Kuwait

Correspondence

Vemula Rajesh, Department of Mathematics, GITAM (Deemed to be University), Hyderabad Campus, Rudraram Village, Patancheru (M), Medak 502329, Telangana, India.
Email: v.rajesh.30@gmail.com

Abstract

The key goals of this manuscript are (i) to investigate the heat transfer and unsteady flow properties of a viscous hybrid nanofluid on a stretching sheet having nonzero slot velocity, and (ii) to examine the impacts of magnetic field parameter, stretching parameter, nanoparticle volume fraction, and heat generation parameter on the Nusselt number and skin friction coefficient numerically. The Tiwari-Das nanofluid model is used. The mathematical (PDEs) equations controlling border layer flow and heat transfer are resolved by applying a numerical finite-difference technique in the Crank Nicolson style. For the validation process, the analytical solution is established using the Laplace transform technique and is compared with the numerical solution for a particular case and found to be in superb agreement.

KEYWORDS

Crank Nicolson finite difference method, heat generation, hybrid nanofluid, MHD, stretching sheet

1 | INTRODUCTION

The transport of momentum, heat, and mass on a running or extending sheet has many functions in polymer processing and electrochemistry.^{1–4} The majority of the research focuses on flow caused by sheets running at a fixed velocity. Crane⁵ primarily investigated the flow produced by an elastic surface, the velocity of which linearly varies with x^* (distance) from a fixed point on the surface. Since that time, several researchers^{6–13} have found the flow, mass, heat transfer issue in the existence or absence of suction (blowing) or magnetic field and have

found solutions of self-similar type. However, it should be noted that the expectation of linear variance of the sheet velocity with distance $v_w = a x^*$ results in an impractical sheet velocity of zero at $x^* = 0$, which is only an approximation to the real problem. Because of this, Jeng et al.¹⁴ studied the flow of nonsimilar types with the stretching sheet's velocity $v_w = a\left(1 + \frac{x^*}{L}\right)$. Takhar et al.¹⁵ researched chemically reactive species and magnetic field impacts on flow and mass transfer using an extending sheet.

Nowadays, heat transfer enrichment is a critical issue for industrial and manufacturing purposes. Most systems use pure fluids as cooling liquids, for instance, ethylene glycol, water, and gasoline, which have poor heat conductivity and restrict heat transfer enrichment. Though, modern varieties of fluids, like nanofluids, are being developed to increase thermal performance. Choi¹⁶ first used nanofluids to contain scattered nanometer-sized particles and the host fluid to produce innovative thermal transfer fluids with significantly elevated conductivities. Nanofluids are commonly employed as lubricants and coolants and in practical products, such as refrigeration, microelectronics, handheld computer processors, and so forth. Several investigators have analyzed the behavior and features of nanofluids in various problems by experimentation and numerically in recent years.^{17–27}

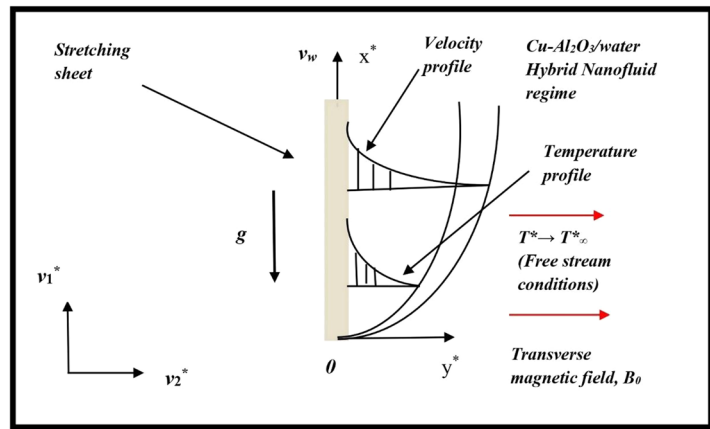
However, researchers are still looking for a better kind of fluid to replace nanofluids, and they have been doing so in recent years. Certain nanofluids known as “hybrid nanofluids” are added to meet the need for a better fluid with high thermal conductivity. With higher performance than nanofluids, hybrid nanofluids are extensively used in various disciplines of thermal transfer, for instance, electrical cooling, reactor cooling, nuclear device cooling, refrigeration, drug reduction, biomedical, and so on. The potential of hybrid nanofluids to improve thermal properties entices researchers to focus on hybrid nanofluids in practical heat transfer problems. Jana et al.²⁸ probed the consequences of hybrid and single nano-additives on fluid heat conductivity. Suresh et al.²⁹ explored the thermal features of an $\text{Al}_2\text{O}_3\text{-Cu/water}$ hybrid nanofluid. Labib et al.³⁰ researched the impact of host liquids and hybrid nanofluids on the heat transfer of forced convective type numerically. Sarkar et al.³¹ provided an overview of hybrid nanofluids: recent science, creation, and implementations. Devi and Devi³² calculated 3D hybrid $\text{Cu-Al}_2\text{O}_3\text{/water}$ nanofluid flow over a broadening sheet with Newtonian heating and Lorentz force. Recently, Waini et al.³³ explored hybrid nanofluid impacts on the unsteady type and heat transfer flow past an extending/dwindling sheet. Other studies of hybrid nanofluids in practical heat transfer problems are described in [34–40].

Given the previous investigative papers and manufacturing and industrial uses, in this study, we have investigated the transient hybrid nanofluid flow and heat transfer features over a continuously stretching surface with an applied magnetic field and heat generation impacts using Cu and Al_2O_3 nanoparticles. The sheet velocity linearly varies with x^* (distance) having the nonzero velocity $\left(v_w = a\left(1 + \frac{x^*}{L}\right)\right)$ at $x^* = 0$. The nonlinear partial differential equations that control border layer flow and heat transfer were numerically answered, applying the implicit finite-difference Crank Nicolson scheme. The results of distinct parameters are analyzed using graphs.

2 | PROBLEM MATHEMATICAL FORMULATION

Let us examine the unsteady, electrically conducting hybrid nanofluid flow of viscous incompressible type on a stretching sheet (surface) in the existence of a magnetic field B_0 employed perpendicular to the sheet. Figure 1 depicts the physical model and the cartesian coordinate system. The sheet and hybrid nanofluid are initially immobile, with the temperature at T_∞^* for all $t^* \leq 0$. Then, the surface

FIGURE 1 The physical model and the coordinate system



is impulsively stretched in the vertically upward direction with a velocity $v_w = a \left(1 + \frac{x^*}{L}\right)$ at time $t^* > 0$. The sheet's surface is maintained at a constant temperature T_w^* greater than the ambient hybrid nanofluid's temperature T_∞^* . Furthermore, it is presumed that the magnetic Reynolds number is negligible. As a result, in this situation, we should disregard the influence of the induced magnetic field in contrast to an applied magnetic field. If the fluid is an electrical insulator, the electrical current passing through it will produce the induced magnetic field; however, we have assumed that the liquid is electrically conducting in this case. As a result, only the applied magnetic field contributes to the generation of magnetic force $F_x = \frac{\sigma_{hnf} B_0^2 v_1^*}{\rho_{hnf}}$. It is assumed that the border layer and Boussinesq approximations⁴¹ are legitimate. The border layer equations handling the flow and temperature fields, following Tiwari and Das¹⁸ nanofluid model, are given by

$$\frac{\partial v_1^*}{\partial x^*} + \frac{\partial v_2^*}{\partial y^*} = 0, \quad (1)$$

$$\frac{\partial v_1^*}{\partial t^*} + v_1^* \frac{\partial v_1^*}{\partial x^*} + v_2^* \frac{\partial v_1^*}{\partial y^*} = \nu_{hnf} \frac{\partial^2 v_1^*}{\partial y^{*2}} + \frac{(\rho\beta)_{hnf}}{\rho_{hnf}} g(T^* - T_\infty^*) - \frac{\sigma_{hnf} B_0^2 v_1^*}{\rho_{hnf}}, \quad (2)$$

$$\frac{\partial T^*}{\partial t^*} + v_1^* \frac{\partial T^*}{\partial x^*} + v_2^* \frac{\partial T^*}{\partial y^*} = \frac{\kappa_{hnf}}{(\rho C_p)_{hnf}} \frac{\partial^2 T^*}{\partial y^{*2}} + \frac{Q_0}{(\rho C_p)_{hnf}} (T^* - T_\infty^*). \quad (3)$$

The associated conditions are

$$\begin{aligned} t^* \leq 0: & \text{ For all } x^* \text{ and } y^*, \quad T^* = T_\infty^*, \quad v_1^* = 0, \quad v_2^* = 0. \\ t^* > 0: & \text{ At } y^* = 0, \quad T^* = T_w^*, \quad v_1^* = v_w(x^*) = a \left(1 + \frac{x^*}{L}\right), \quad v_2^* = 0. \\ & \text{ At } x^* = 0, \quad T^* = T_\infty^*, \quad v_1^* = 0, \\ & \text{ As } y^* \rightarrow \infty, \quad T^* \rightarrow T_\infty^*, \quad v_1^* \rightarrow 0, \end{aligned} \quad (4)$$

where a is a constant velocity (with $a > 0$) and has dimension: length. time⁻¹ (LT⁻¹). The critical thermal physical features of hybrid nanofluid, water, and nanoadditives are listed in Tables 1 and 2.

TABLE 1 Thermophysical features of $Cu - Al_2O_3$ /water

Property	Hybrid nanofluid (CU- Al_2O_3 /water)
Density (ρ)	$\rho_{hnf} = [(1 - \varphi_2)\{(1 - \varphi_1)\rho_f + \varphi_1\rho_{s1}\}] + \varphi_2\rho_{s2}$
Dynamic viscosity (μ)	$\mu_{hnf} = \frac{\mu_f}{(1 - \varphi_1)^{2.5}(1 - \varphi_2)^{2.5}}$
Heat capacity (ρC_p)	$(\rho C_p)_{hnf} = [(1 - \varphi_2)\{(1 - \varphi_1)(\rho C_p)_f + \varphi_1(\rho C_p)_{s1}\}] + \varphi_2(\rho C_p)_{s2}$
Thermal expansion coefficient ($\rho\beta$)	$(\rho\beta)_{hnf} = [(1 - \varphi_2)\{(1 - \varphi_1)(\rho\beta)_f + \varphi_1(\rho\beta)_{s1}\}] + \varphi_2(\rho\beta)_{s2}$
Thermal Conductivity (κ)	$\kappa_{hnf} = \kappa_{nf} \frac{\kappa_{s2} + (n_1 - 1)\kappa_{nf} - (n_1 - 1)\varphi_2(\kappa_{nf} - \kappa_{s2})}{\kappa_{s2} + (n_1 - 1)\kappa_{nf} + \varphi_2(\kappa_{nf} - \kappa_{s2})}$, where $\kappa_{nf} = \kappa_f \frac{\kappa_{s1} + (n_1 - 1)\kappa_f - (n_1 - 1)\varphi_1(\kappa_f - \kappa_{s1})}{\kappa_{s1} + (n_1 - 1)\kappa_f + \varphi_1(\kappa_f - \kappa_{s1})}$
Electrical conductivity	$\sigma_{hnf} = \sigma_{nf} \left[\frac{\sigma_{s2}(1 + 2\varphi_2) + 2\sigma_{nf}(1 - \varphi_2)}{\sigma_{s2}(1 - \varphi_2) + \sigma_{nf}(2 + \varphi_2)} \right]$, where $\sigma_{nf} = \sigma_f \left[\frac{\sigma_{s1}(1 + 2\varphi_1) + 2\sigma_f(1 - \varphi_1)}{\sigma_{s1}(1 - \varphi_1) + \sigma_f(2 + \varphi_1)} \right]$

TABLE 2 Thermophysical features of water and nanoparticles

	ρ (kg/m ³)	κ (W/mK)	σ (s/m)	β (1/K)	C_p (J/kg K)
H_2O (f)	997.1	0.613	5.5×10^{-6}	21×10^{-5}	4179
Cu (s2)	8933	401	59.6×10^6	1.67×10^{-5}	385
Al_2O_3 (s1)	3970	40	35×10^6	0.85×10^{-5}	765

Source: Turkyilmazoglu.⁴²

Using the below-mentioned transformations

$$x = \frac{x^*}{L}, y = \frac{y^* G_r^{1/4}}{L}, v_1 = \frac{v_1^* L}{\nu_f} G_r^{-1/2}, v_2 = \frac{v_2^* L}{\nu_f} G_r^{-1/4}, t = \frac{\nu_f t^*}{L^2} G_r^{1/2}, \vartheta = \frac{T^* - T_\infty^*}{T_w^* - T_\infty^*} \quad (5)$$

into Equations (1), (2) and (3) we get

$$\frac{\partial v_1}{\partial x} + \frac{\partial v_2}{\partial y} = 0, \quad (6)$$

$$\frac{\partial v_1}{\partial t} + v_1 \frac{\partial v_1}{\partial x} + v_2 \frac{\partial v_1}{\partial y} = \frac{F_2}{F_1} \frac{\partial^2 v_1}{\partial y^2} + \frac{F_3}{F_1} \vartheta - \frac{F_4}{F_1} M v_1, \quad (7)$$

$$\frac{\partial \vartheta}{\partial t} + v_1 \frac{\partial \vartheta}{\partial x} + v_2 \frac{\partial \vartheta}{\partial y} = \frac{F_6}{F_5} \frac{1}{Pr} \frac{\partial^2 \vartheta}{\partial y^2} + \frac{Q}{F_5} \vartheta. \quad (8)$$

The corresponding conditions relations are

$$\begin{aligned} t \leq 0: & \text{ For all } x \text{ and } y, \vartheta = 0, v_1 = 0, v_2 = 0. \\ t > 0: & \text{ At } y = 0, \vartheta = 1, v_1 = A(1 + x), v_2 = 0. \\ & \text{ At } x = 0, \vartheta = 0, v_1 = 0, \\ & \text{ As } y \rightarrow \infty, \vartheta \rightarrow 0, v_1 \rightarrow 0. \end{aligned} \quad (9)$$

Here $Pr = \frac{\nu_f}{\alpha_f}$ (Prandtl number), $Gr = \frac{8\beta_f L^3(T_w^* - T_\infty^*)}{\nu_f^2}$ (Grashof number), $M = \frac{\sigma_f B_0^2 L^2}{\rho_f \nu_f} Gr^{-1/2}$ (magnetic parameter), $Q = \frac{Q_0 L^2}{\mu_f (C_p)_f} Gr^{-1/2}$ (heat generation parameter), $A = \frac{aL}{\nu_f} Gr^{-1/2}$ (stretching parameter), L is the reference length and

$$\begin{aligned}
 F_1 &= [(1 - \varphi_2)\{(1 - \varphi_1) + \varphi_1 \rho_{s1}/\rho_f\}] + \varphi_2 \rho_{s2}/\rho_f, & F_2 &= 1/(1 - \varphi_1)^{2.5}(1 - \varphi_2)^{2.5} \\
 F_3 &= \left[(1 - \varphi_2) \left\{ (1 - \varphi_1) + \varphi_1 \frac{(\rho\beta)_{s1}}{(\rho\beta)_f} \right\} \right] + \varphi_2 \frac{(\rho\beta)_{s2}}{(\rho\beta)_f}, & F_4 &= \frac{\sigma_{nf}}{\sigma_f} \left[\frac{\sigma_{s2}(1 + 2\varphi_2) + 2\sigma_{nf}(1 - \varphi_2)}{\sigma_{s2}(1 - \varphi_2) + \sigma_{nf}(2 + \varphi_2)} \right] \\
 F_5 &= \left[(1 - \varphi_2) \left\{ (1 - \varphi_1) + \varphi_1 \frac{(\rho C_p)_{s1}}{(\rho C_p)_f} \right\} \right] + \varphi_2 \frac{(\rho C_p)_{s2}}{(\rho C_p)_f}, \\
 F_6 &= \frac{\kappa_{nf} [\kappa_{s2} + (n_1 - 1)\kappa_{nf} - (n_1 - 1)\varphi_2(\kappa_{nf} - \kappa_{s2})]}{\kappa_f [\kappa_{s2} + (n_1 - 1)\kappa_{nf} + \varphi_2(\kappa_{nf} - \kappa_{s2})]}.
 \end{aligned}
 \tag{10}$$

FIGURE 2 Mesh sensitivity analysis

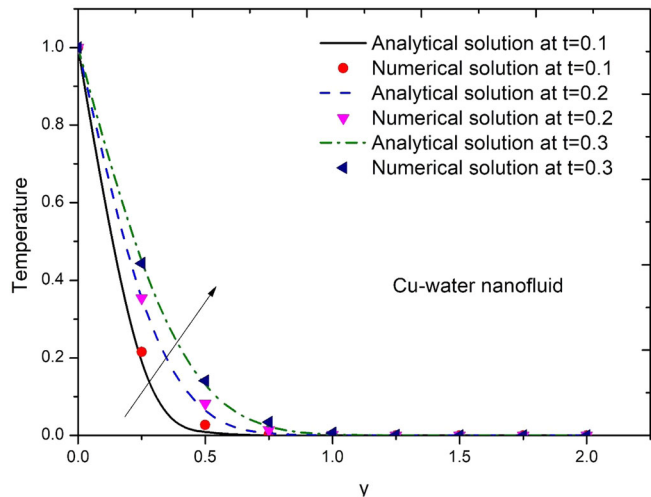
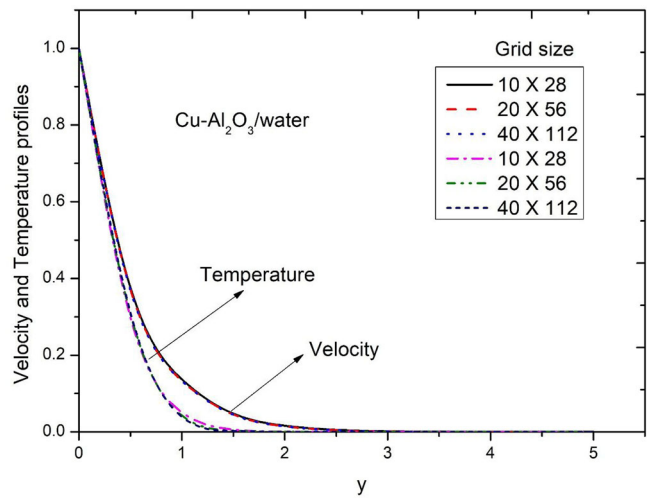


FIGURE 3 Validation of the numerical technique

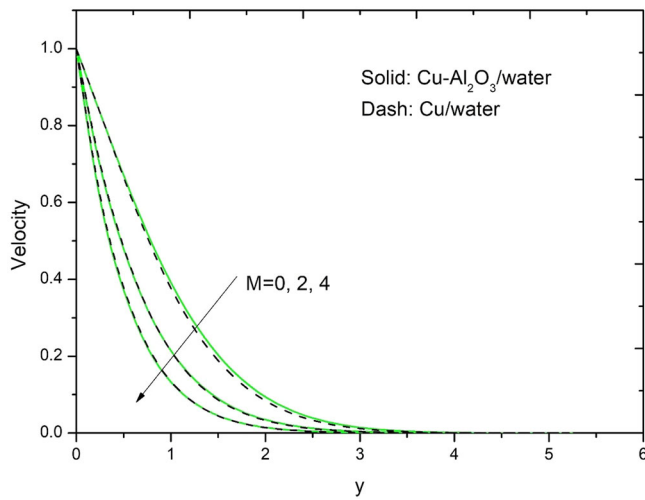


FIGURE 4 Velocity patterns with y for M

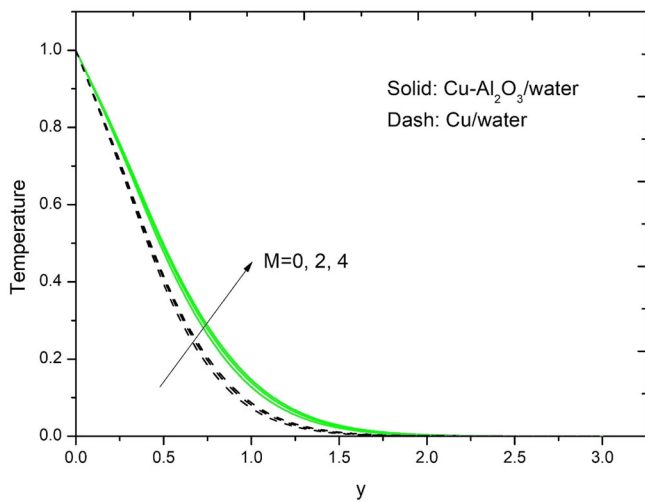


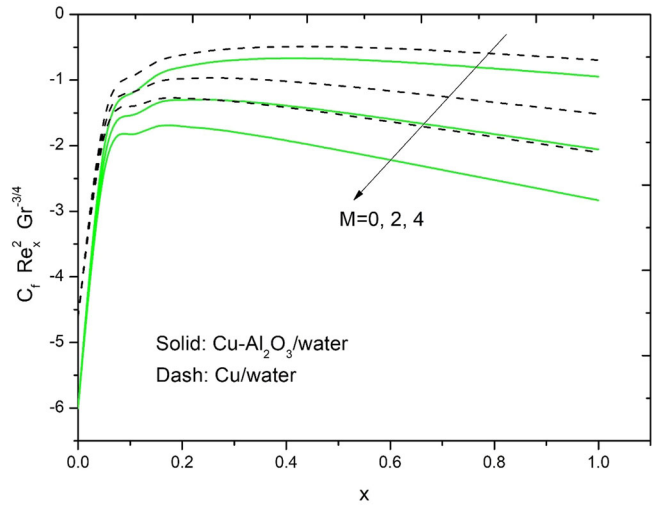
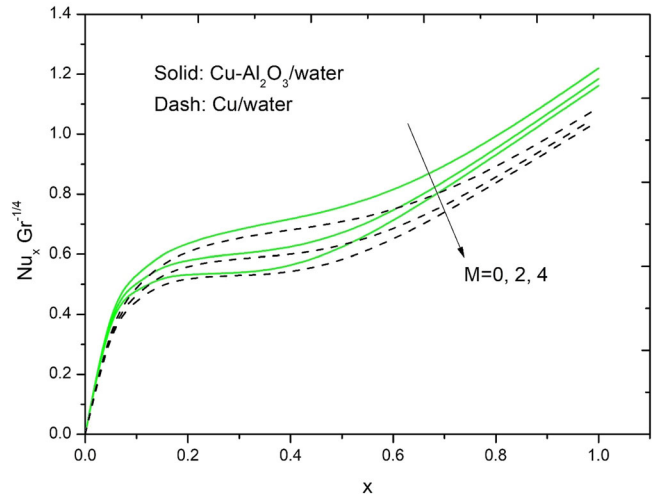
FIGURE 5 Temperature profiles with y for M

In the absence of heat generation and inertial terms, Equation (8) reduces to

$$\frac{\partial \vartheta}{\partial t} = \frac{F_6}{F_5} \frac{1}{Pr} \frac{\partial^2 \vartheta}{\partial y^2}. \quad (11)$$

The exact result of Equation (11) relying on the constraints (9), is given by the analytical (Laplace transform) method

$$\vartheta = \operatorname{erfc} \left(\frac{y}{2} \sqrt{\frac{Pr}{t}} \frac{F_6}{F_5} \right). \quad (12)$$

FIGURE 6 Skin friction coefficient with x for M **FIGURE 7** Nusselt number with x for M 

2.1 | Engineering quantities

The valuable quantities viz C_f (skin friction parameter) and Nu_x , (local Nusselt number) specified as

$$C_f = \frac{\tau_w}{\rho_f v_w^2}, Nu_x = \frac{q_w x^*}{\kappa_f (T_w^* - T_\infty^*)}, \quad (13)$$

where τ_w (skin-friction) and q_w (heat transfer) from the surface are presented by

$$\tau_w = \mu_{hnf} \left(\frac{\partial v_1^*}{\partial y^*} \right)_{y^*=0}, q_w = -\kappa_{hnf} \left(\frac{\partial T^*}{\partial y^*} \right)_{y^*=0}. \quad (14)$$

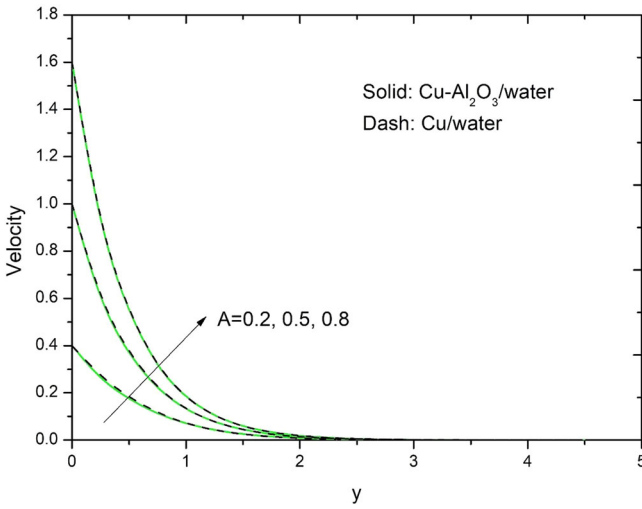


FIGURE 8 Velocity profiles with y for A

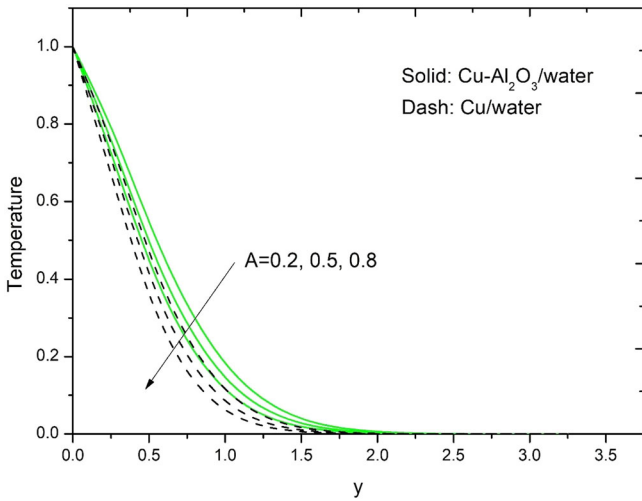


FIGURE 9 Temperature profiles with y for A

Employing transformations (5), we get

$$C_f Re_x^2 = \frac{1}{(1 - \phi_1)^{2.5}(1 - \phi_2)^{2.5}} G_r^{3/4} \left(\frac{\partial v_1}{\partial y} \right)_{y=0}, Nu_x = -\frac{\kappa_{hnf}}{\kappa_f} G_r^{1/4} x \left(\frac{\partial \theta}{\partial y} \right)_{y=0}, \quad (15)$$

where $Re_x = \frac{v_w L}{\nu_f}$ is the Reynolds number.

FIGURE 10 Skin friction coefficient with x for A

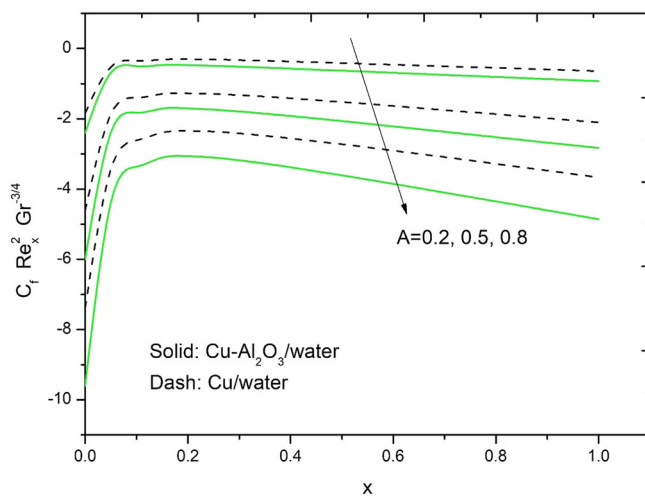


FIGURE 11 Nusselt number with x for A

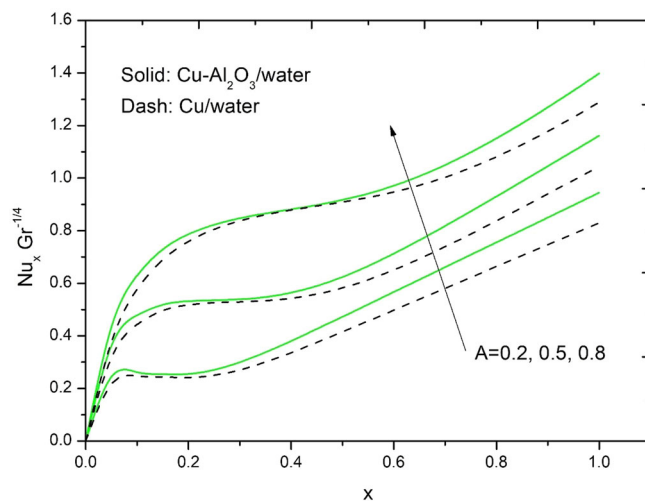
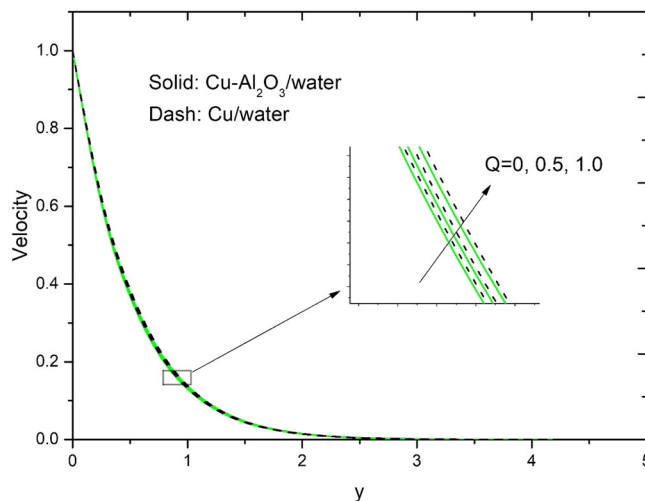


FIGURE 12 Velocity patterns with y for Q



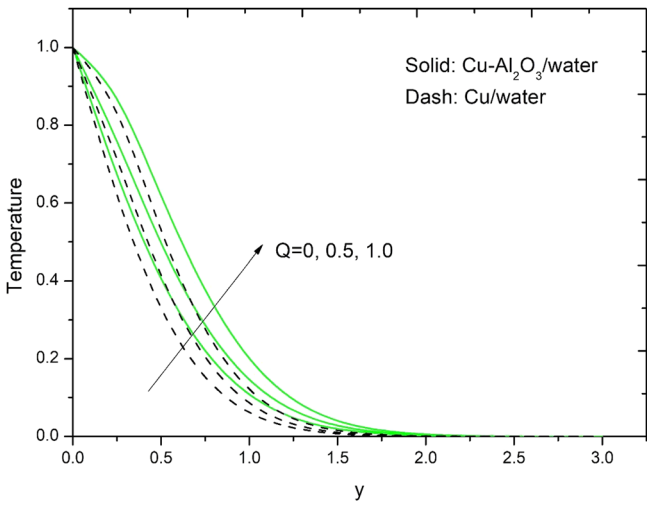


FIGURE 13 Temperature patterns with y for Q

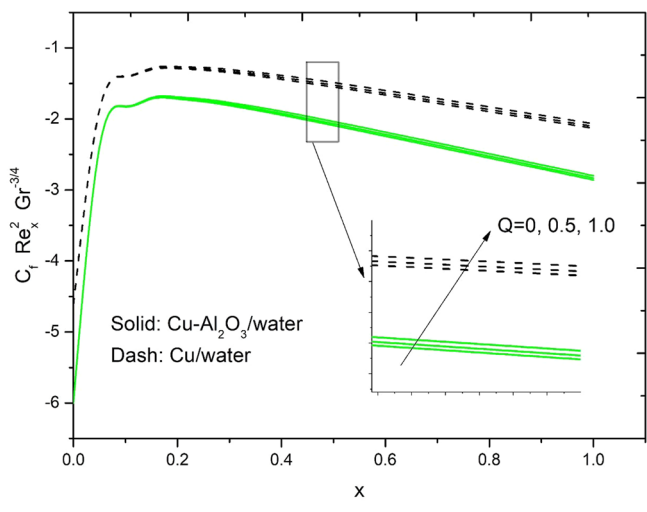


FIGURE 14 Skin friction coefficient with x for Q

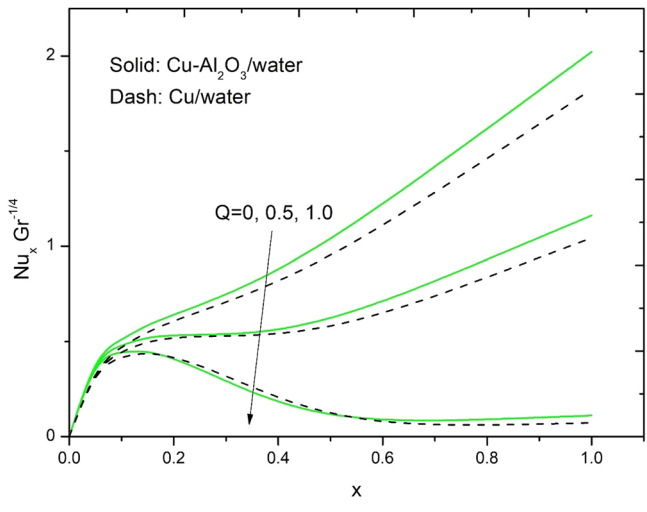


FIGURE 15 Nusselt number with x for Q

84512, 2022, 4, Downloaded from https://onlinelibrary.wiley.com/doi/10.1002/htj.22427 by University Of Toronto Mississauga, Wiley Online Library on [24/11/2022]. See the Terms and Conditions (https://onlinelibrary.wiley.com/terms-and-conditions) on Wiley Online Library for rules of use; OA articles are governed by the applicable Creative Commons License

FIGURE 16 Velocity patterns with y for ϕ_2

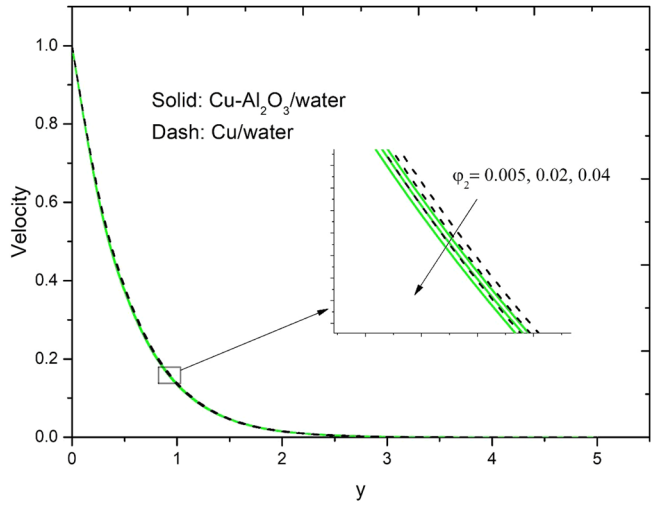
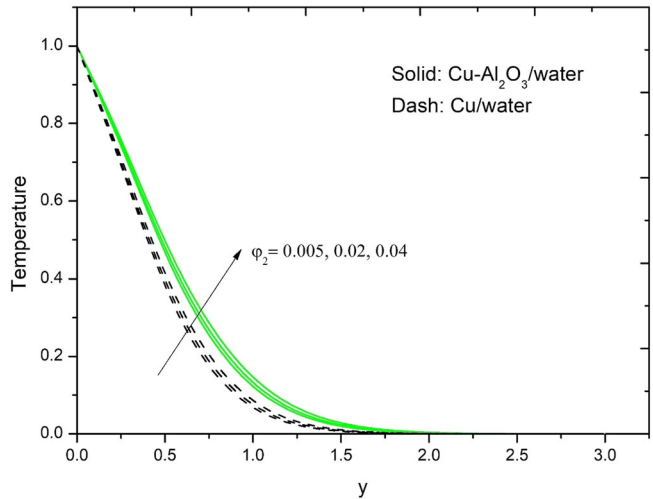


FIGURE 17 Temperature patterns with y for ϕ_2



3 | NUMERICAL METHOD OF SOLUTION

The PDEs (6)–(8) and the linked conditions (9) were cracked using a strong Crank-Nicolson style numerical procedure. The respective difference equalities are as follows:

$$\left[\frac{(v_1)_{ij}^{n+1} - (v_1)_{i-1,j}^{n+1} + (v_1)_{ij}^n - (v_1)_{i-1,j}^n + (v_1)_{ij-1}^{n+1} - (v_1)_{i-1,j-1}^{n+1} + (v_1)_{ij-1}^n - (v_1)_{i-1,j-1}^n}{4\Delta x} \right] + \left[\frac{(v_2)_{ij}^{n+1} - (v_2)_{i,j-1}^{n+1} + (v_2)_{ij}^n - (v_2)_{i,j-1}^n}{2\Delta y} \right] = 0, \quad (16)$$

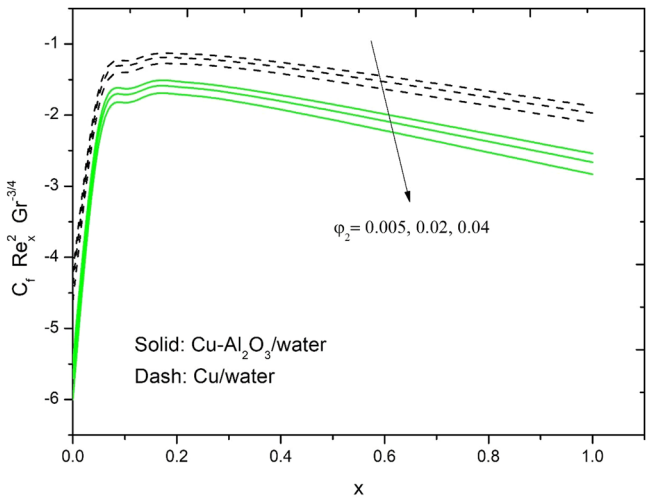


FIGURE 18 Skin friction coefficient with x for ϕ_2

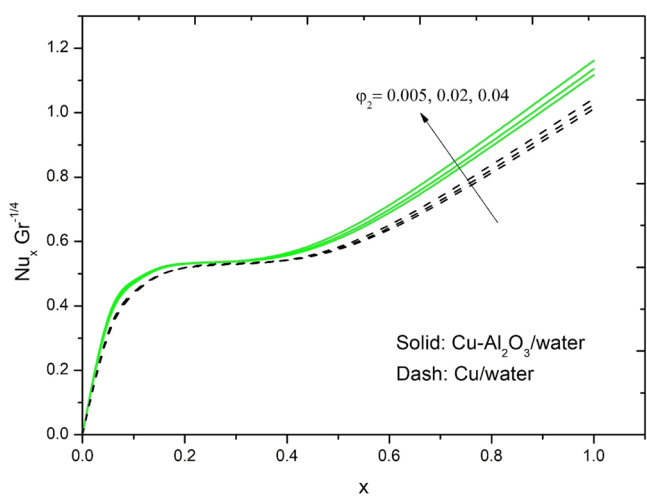


FIGURE 19 Nusselt number with x for ϕ_2

$$\left[\frac{(v_1)_{i,j}^{n+1} - (v_1)_{i,j}^n}{\Delta t} \right] + (v_1)_{i,j}^n \left[\frac{(v_1)_{i,j}^{n+1} - (v_1)_{i-1,j}^{n+1} + (v_1)_{i,j}^n - (v_1)_{i-1,j}^n}{2\Delta x} \right] + (v_2)_{i,j}^n \left[\frac{(v_1)_{i,j+1}^{n+1} - (v_1)_{i,j-1}^{n+1} + (v_1)_{i,j+1}^n - (v_1)_{i,j-1}^n}{4\Delta y} \right] \tag{17}$$

$$= \frac{F_3}{F_1} \frac{1}{2} \left[\vartheta_{i,j}^{n+1} + \vartheta_{i,j}^n \right] + \frac{F_2}{F_1} \left[\frac{(v_1)_{i,j-1}^{n+1} - 2(v_1)_{i,j}^{n+1} + (v_1)_{i,j+1}^{n+1} + (v_1)_{i,j-1}^n - 2(v_1)_{i,j}^n + (v_1)_{i,j+1}^n}{2(\Delta y)^2} \right] - \frac{F_4 M}{F_1} \frac{1}{2} \left[(v_1)_{i,j}^{n+1} + (v_1)_{i,j}^n \right],$$

$$\left[\frac{\vartheta_{i,j}^{n+1} - \vartheta_{i,j}^n}{\Delta t} \right] + (v_1)_{i,j}^n \left[\frac{\vartheta_{i,j}^{n+1} - \vartheta_{i-1,j}^{n+1} + \vartheta_{i,j}^n - \vartheta_{i-1,j}^n}{2\Delta x} \right] + (v_2)_{i,j}^n \left[\frac{\vartheta_{i,j+1}^{n+1} - \vartheta_{i,j-1}^{n+1} + \vartheta_{i,j+1}^n - \vartheta_{i,j-1}^n}{4\Delta y} \right] \tag{18}$$

$$= \frac{F_6}{F_5} \left[\frac{\vartheta_{i,j-1}^{n+1} - 2\vartheta_{i,j}^{n+1} + \vartheta_{i,j+1}^{n+1} + \vartheta_{i,j-1}^n - 2\vartheta_{i,j}^n + \vartheta_{i,j+1}^n}{2Pr(\Delta y)^2} \right] + \frac{Q}{2F_5} \left[\vartheta_{i,j}^{n+1} + \vartheta_{i,j}^n \right].$$

FIGURE 20 Velocity patterns with y for t

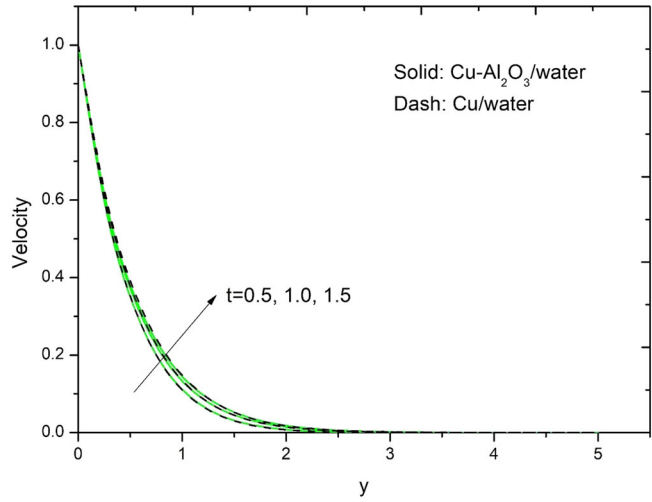
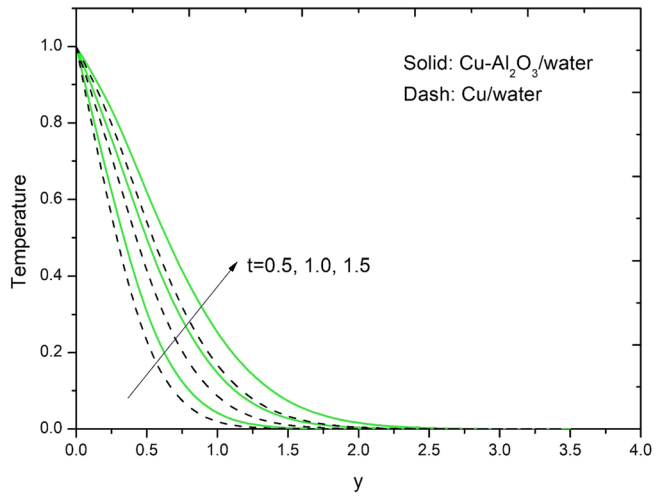


FIGURE 21 Temperature patterns with y for t



The Thomas algorithm⁴³ searches the previous equations for numerical answers to velocity and temperature fields. Additional details of the method viz consistency, stability, and convergence are provided in Ramachandra Prasad et al.⁴⁴ Figure 2 depicts mesh sensitivity analysis results used to determine the best mesh structure for numerical simulation. To obtain accurate results, the steps $\Delta x = 0.05$ for the x -axis and $\Delta y = 0.25$ for the y -axis were described. Simultaneously, the time step was investigated, with $\Delta t = 0.01$ selected as the best value for good outcomes. The temperature trends from this analysis (when $\varphi_1 = 0$, $Q = 0$, $M = 0$, $A = 0$) are compared with the exact solution (12) in Figure 3 to ensure the numerical results' precision, which is seen to be excellent. This suggests that the current solution approach is suitable for this kind of issue.

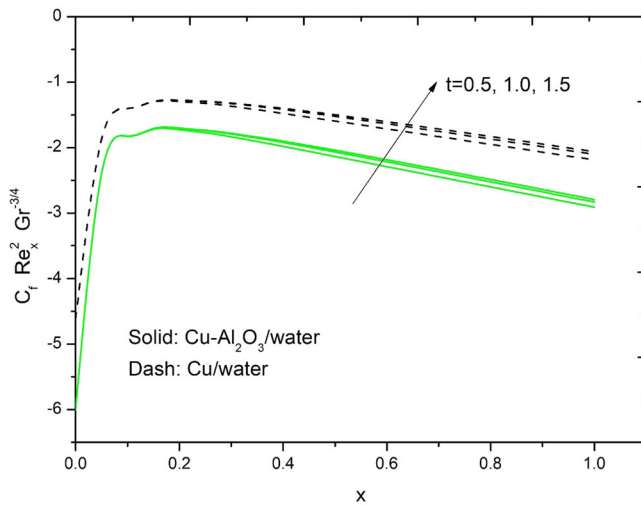


FIGURE 22 Skin friction coefficient with x for t

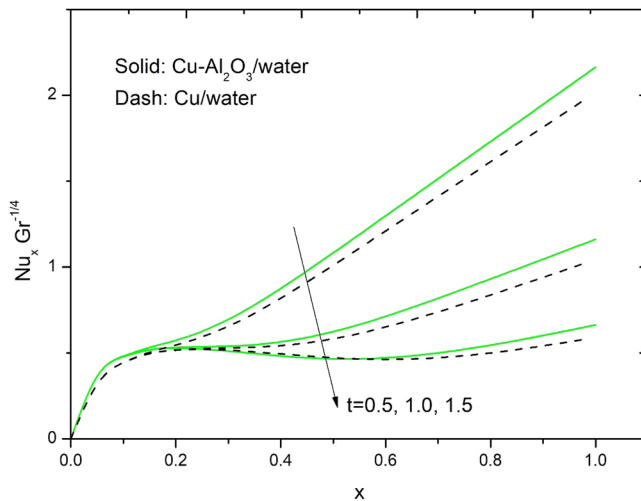


FIGURE 23 Nusselt number with x for t

4 | RESULTS AND DISCUSSION

The Crank Nicolson method is used to conduct computational simulations for different sets of related parameters, namely magnetic parameter ($M = 0, 2, 4$), stretching parameter ($A = 0.2, 0.5, 0.8$), heat generation parameter ($Q = 0, 0.5, 1$), and nanoparticle volume fraction ($\varphi_2 = 0.005, 0.02, 0.04$). The results are shown in Figures 4–23 to show how diverse limits influence heat transfer and transient flow features. Except otherwise defined, we assume $M = 4$, $A = 0.5$, $Q = 0.5$, $\varphi_1 = 0.1$, $\varphi_2 = 0.04$, $Pr = 6.2$, $t = 1$, $n_1 = 3$, and $X = 1$ to be constants in the current analysis.

Figures 4–7 show how M (magnetic field parameter) affects velocity, skin friction coefficient, temperature, and Nusselt number for nano and hybrid nanofluids. Figure 4 shows that increasing M causes a decline in velocity and the thickness of the border layer since increasing M causes a Lorentz force that opposes the fluid flow. However, as seen in Figure 5, the temperature rises as M increases. Furthermore, for all M , the temperature border layer thickness of $\text{Cu-Al}_2\text{O}_3/\text{Water}$ is bigger than that of Cu/Water . Figures 6 and 7 demonstrate that as M increases, both engineering quantities C_f

(skin friction parameter) and Nu_x (local Nusselt number) decrease. Using Cu/Al₂O₃-water hybrid nanofluid as a working medium, we can minimize C_f and increase Nu_x compared with Cu-water nanofluid, as shown in Figures 6 and 7.

Figures 8–11 reveal the velocity and temperature variations with y and the engineering quantities viz skin friction coefficient and Nusselt number variations with x for different A (stretching parameter) values for nano and hybrid nanofluid situations. Figure 8 shows that velocity increases with increasing A for both fluids since increasing A increases the flow rate in the boundary layer. However, with all fluids, temperature and border layer thickness decrease as A rises, as shown in Figure 9. Further, Figure 9 shows that the temperature border layer thickness of Cu/Al₂O₃-water is bigger than that of Cu-water. Figures 10 and 11 show that as A increases, the C_f (skin friction coefficient) decreases and the Nu_x (Nusselt number) increases. Further, Figures 10 and 11 demonstrate that similar to the effect of M , using Cu/Al₂O₃-water rather than Cu-water results in higher Nu_x and lower C_f values for all A . Figures 12–15 show the effect of Q (heat generation parameter) on velocity, skin friction coefficient, temperature, and Nusselt number for both fluids of nano and hybrid situations. Figures 12 and 13 demonstrate that as Q increases, so do velocity and temperature since increasing Q causes an increase in temperature gradient and buoyancy force. Figures 14 and 15 show how increasing Q caused an increase in skin friction coefficient and a decrease in Nusselt number.

The impact of φ_2 (nanoparticle volume fraction) on velocity, temperature, skin friction coefficient, and Nusselt number are investigated in Figures 16–19. Figure 16 shows that as φ_2 increases, the velocity decreases. This is because increasing φ_2 increases the viscosity of the liquid, which slows down the liquid flow. However, as seen in Figure 17, the temperature rises as φ_2 increases. The explanation for this is that nanoparticles dissipate heat. This is boosted even more by the inclusion of more particles. Furthermore, the temperature boundary layer thickness of hybrid nanofluid is bigger than that of nanofluid. In Figures 18 and 19, it is apparent that Cu/Al₂O₃-water has a higher Nu_x (Nusselt number) and a lower C_f (skin friction coefficient) than Cu-water. Figures 20–23 show the variations in velocity, skin friction coefficient, temperature, and Nusselt number with rising t . The data shows that while velocity, temperature, and skin friction coefficient rise over time, the Nusselt number declines. Also, the velocity and temperature border layer thicknesses of both fluids grow over time. In addition, hybrid nanofluid has a thicker temperature boundary layer than nanofluid. We will minimize skin friction coefficient by using hybrid type nanofluid as a working medium instead of nanofluid for all t .

5 | CONCLUSIONS

This paper investigated the effects of MHD and heat generation on the transient flow and heat transfer of hybrid nanofluid on a stretching surface with nonzero slot velocity numerically. The study's key conclusions are as follows:

1. Velocity decreased with rising M or φ_2 , while increased with growing A or Q or t for both fluids.
2. Temperature raises with increasing M or φ_2 or Q or t , and falls with growing A for both fluids.
3. Decay in the skin friction coefficient is found with rising M or φ_2 or A , while an increase is found with increasing Q or t .
4. The Nusselt number rises with increasing A and falls with growing M or t or Q .

5. For all M or A or ϕ_2 , the heat transfer rate for Cu–Al₂O₃/water is more significant than Cu/water.
6. For all M or A or ϕ_2 or t or Q , the skin friction coefficient values of Cu–Al₂O₃/water are more petite than Cu/water.

NOMENCLATURE

v_1^*	velocity x - component (m s^{-1})
ϕ_1	aluminium oxide nanoparticles concentration
ϕ_2	copper nanoparticles concentration
μ	dynamic viscosity (Pa s)
T_∞^*	temperature of liquid far away from the sheet
ϑ	nondimensional temperature
ρ	density (kg m^{-3})
T_w^*	sheet temperature (K)
v_2^*	velocity y -component (m s^{-1})
κ	heat conductivity ($\text{W m}^{-1} \text{K}^{-1}$)
Δx	grid step size in x -direction
ν	kinematic viscosity ($\text{m}^2 \text{s}^{-1}$)
β	volumetric thermal expansion coefficient (K^{-1})
Δt	time grid step size
g	acceleration (owing to gravity) (m s^{-2})
n_1	nanoadditives empirical form parameter
Δy	grid step size in y -direction
Nu_x	local Nusselt number
Pr	prandtl number
C_p	specific heat (at constant pressure) ($\text{J kg}^{-1} \text{K}^{-1}$)
t	nondimensional time
T^*	liquid temperature (K)
t^*	time (s)
x	dimensionless cartesian coordinate parallel to the sheet
x^*	cartesian coordinate parallel the sheet (m)
v_1	dimensionless velocity x -component
v_2	dimensionless velocity y -component
y	dimensionless cartesian coordinate perpendicular to the sheet
y^*	cartesian coordinate perpendicular to the sheet (m)

SUBSCRIPTS

w	sheet surface conditions
∞	free stream conditions
f	base fluid
i	x -direction mesh node
j	y -direction mesh node
nf	nanofluid
hnf	hybrid nanofluid
$s1$	aluminium oxide nanoparticles
$s2$	copper nanoparticles

SUPERSCRIPTS

n time grid node

REFERENCES

- Griffith RM. Velocity temperature and concentration distributions during fibre spinning. *Ind Eng Chem Fundam.* 1964;3(3):245-250.
- Erickson LE, Fan LT. VGF. Heat and mass transfer on a moving continuous flat plate with suction or injection. *Ind Eng Chem Fundam.* 1966;5(1):19-25.
- Chin D-T. Mass transfer to a continuous moving sheet electrode. *J Electrochem Soc Electrochem Sci Technol.* 1975;122(5):643-646.
- Gorla RSR. Unsteady mass transfer in the boundary layer on a continuous moving sheet electrode. *J Electrochem Soc.* 1978;125(6):865-869.
- Crane LJ. Flow past a stretching plate. *Kurze Mitteilungen—Br Reports—Commun breves.* 1970;21:645-647.
- Vlegaar J. Laminar boundary-layer behaviour on continuous, accelerating surfaces. *Chem Eng Sci.* 1977;32(12):1517-1525.
- Gupta PS, Gupta AS. Heat and mass transfer on a stretching sheet with suction or blowing. *Can J Chem Eng.* 1977;55:744-746.
- Chakrabarti A, Gupta AS. Hydromagnetic flow and heat transfer over a stretching sheet. *Q Appl Math.* 1979;37(1):73-78.
- Carragher P, Crane LJ. Heat transfer on a continuous stretching sheet. *ZAMM—J Appl Math Mech/Zeitschrift für Angew Math und Mech.* 1982;62(10):564-565.
- Grubka LJ, Bobba KM. Heat transfer characteristics of a continuous, stretching surface with variable. *Temperature.* 1985;107:248-250.
- Chen CK, Char MI. Heat transfer of a continuous, stretching surface with suction or blowing. *J Math Anal Appl.* 1988;135(2):568-580.
- Dutta BK. Heat transfer from a stretching sheet with uniform suction and blowing. *Acta Mech.* 1989;78(3-4):255-262.
- Andersson HI. An exact solution of the Navier-Stokes equations for magnetohydrodynamic flow. *Acta Mech.* 1995;113(1-4):241-244.
- Jeng DR, Chang TCA, De, Witt KJ. Momentum and heat transfer on a continuous moving surface. *J Heat Transfer.* 1986;108(3):532-539.
- Takhar HS, Chamkha AJ, Nath G. Flow and mass transfer on a stretching sheet with a magnetic field and chemically reactive species. *Int J Eng Sci.* 2000;38(12):1303-1314.
- Choi SUS. Enhancing thermal conductivity of fluids with nanoparticles. *Am Soc Mech Eng Fluids Eng Div FED.* 1995;231(March):99-105.
- Buongiorno J. Convective transport in nanofluids. *J Heat Transfer.* 2006;128(3):240-250.
- Tiwari RK, Das MK. Heat transfer augmentation in a two-sided lid-driven differentially heated square cavity utilizing nanofluids. *Int J Heat Mass Transf.* 2007;50(9-10):2002-2018.
- Hwang KS, Lee JH, Jang SP. Buoyancy-driven heat transfer of water-based Al₂O₃ nanofluids in a rectangular cavity. *Int J Heat Mass Transf.* 2007;50(19-20):4003-4010.
- Das SK, Choi SUS, Yu TP W. *Nanofluids: Science and Technology.* Wiley-Interscience; 2007.
- Trisaksri V, Wongwises S. Critical review of heat transfer characteristics of nanofluids. *Renew Sustain Energy Rev.* 2007;11(3):512-523.
- Kuznetsov AV, Nield DA. Natural convective boundary-layer flow of a nanofluid past a vertical plate. *Int J Therm Sci.* 2010;49(2):243-247. doi:10.1016/j.ijthermalsci.2009.07.015
- Khan WA, Aziz A. Natural convection flow of a nanofluid over a vertical plate with uniform surface heat flux. *Int J Therm Sci.* 2011;50(7):1207-1214.
- Bachok N, Ishak A, Pop I. Flow and heat transfer characteristics on a moving plate in a nanofluid. *Int J Heat Mass Transf.* 2012;55(4):642-648. doi:10.1016/j.ijheatmasstransfer.2011.10.047
- Rajesh V, Bég OA. MHD transient nanofluid flow and heat transfer from a moving vertical cylinder with temperature oscillation. *Comput Therm Sci.* 2014;6(5):439-450.

26. Vemula R, Chamkha A, Mallesh MP. Nanofluid flow past an impulsively started vertical plate with variable surface temperature. *Int J Numer Methods Heat Fluid Flow*. 2016;26(1):328-347.
27. Rajesh V, Chamkha AJ, Sridevi C, Al-Mudhaf AF. A numerical investigation of transient MHD free convective flow of a nanofluid over a moving semi-infinite vertical cylinder. *Eng Comput (Swansea, Wales)*. 2017;34(5):1393-1412.
28. Jana S, Salehi-Khojin A, Zhong WH. Enhancement of fluid thermal conductivity by the addition of single and hybrid nano-additives. *Thermochim Acta*. 2007;462(1-2):45-55.
29. Suresh S, Venkataraj KP, Selvakumar P, Chandrasekar M. Effect of Al₂O₃-Cu/water hybrid nanofluid in heat transfer. *Exp Therm Fluid Sci*. 2012;38:54-60. doi:10.1016/j.expthermflusci.2011.11.007
30. Nuim Labib M, Nine MJ, Afrianto H, Chung H, Jeong H. Numerical investigation on effect of base fluids and hybrid nanofluid in forced convective heat transfer. *Int J Therm Sci*. 2013;71:163-171. doi:10.1016/j.ijthermalsci.2013.04.003
31. Sarkar J, Ghosh P, Adil A. A review on hybrid nanofluids: recent research, development and applications. *Renew Sustain Energy Rev*. 2015;43:164-177. doi:10.1016/j.rser.2014.11.023
32. Devi SSU, Devi SPA. Numerical investigation of three-dimensional hybrid Cu-Al₂O₃/water nanofluid flow over a stretching sheet with effecting Lorentz force subject to Newtonian heating. *Can J Phys*. 2016;94(5):490-496.
33. Waini I, Ishak A, Pop I. Unsteady flow and heat transfer past a stretching/shrinking sheet in a hybrid nanofluid. *Int J Heat Mass Transf*. 2019;136:288-297. doi:10.1016/j.ijheatmasstransfer.2019.02.101
34. Vafaei M, Afrand M, Sina N, Kalbasi R, Sourani F, Teimouri H. Evaluation of thermal conductivity of MgO-MWCNTs/EG hybrid nanofluids based on experimental data by selecting optimal artificial neural networks. *Phys E Low Dimens Syst Nanostruct*. 2017;85:90-96. doi:10.1016/j.physe.2016.08.020
35. Tayebi T, Chamkha AJ. Buoyancy-driven heat transfer enhancement in a sinusoidally heated enclosure utilizing hybrid nanofluid. *Comput Therm Sci*. 2017;9(5):405-421.
36. Ghalambaz M, Sheremet MA, Mehryan SAM, Kashkooli FM, Pop I. Local thermal non-equilibrium analysis of conjugate free convection within a porous enclosure occupied with Ag-MgO hybrid nanofluid. *J Therm Anal Calorim*. 2019;135(2):1381-1398. doi:10.1007/s10973-018-7472-8
37. Hayat T, Nadeem S, Khan AU. Rotating flow of Ag-CuO/H₂O hybrid nanofluid with radiation and partial slip boundary effects. *Eur Phys J E*. 2018;41(6):75.
38. Huminic G, Huminic A. Hybrid nanofluids for heat transfer applications—a state-of-the-art review. *Int J Heat Mass Transf*. 2018;125:82-103. doi:10.1016/j.ijheatmasstransfer.2018.04.059
39. Vemula R, Kavitha M, Sheremet MA. Effects of internal heat generation and Lorentz force on unsteady hybrid nanofluid flow and heat transfer along a moving plate with nonuniform temperature. *Heat Transf*. 2021;50(3):2975-2996.
40. Rajesh V, Chamkha A, Kavitha M. Numerical investigation of Ag-CuO/water hybrid nanofluid flow past a moving oscillating cylinder with heat transfer. *Math Methods Appl Sci*. 2020;(May):13-17.
41. Herrmann Schlichting KG. *Boundary-Layer Theory*. Springer Berlin Heidelberg; 2000.
42. Turkyilmazoglu M. Unsteady convection flow of some nanofluids past a moving vertical flat plate with heat transfer. *J Heat Transfer*. 2014;136(3):1-7.
43. Carnahan B, Luther HA, Wilkes WO. *Applied Numerical Methods*, 1969.
44. Prasad VR, Reddy NB, Muthucumaraswamy R. Radiation and mass transfer effects on two-dimensional flow past an impulsively started infinite vertical plate. *Int J Therm Sci*. 2007;46(12):1251-1258.

How to cite this article: Rajesh V, Srilatha M, Chamkha AJ. Numerical study of hybrid nanofluid flow and heat transfer on a stretching sheet with MHD and heat generation effects. *Heat Transfer*. 2022;51:2867-2884. doi:10.1002/htj.22427